AREA
CA
SnBen
FINH

FAULT INTERACTION NEAR HOLLISTER, CALIFORNIA

Gerald M. Mavko

U. S. Geological Survey

Menlo Park, California

(Short title: Fault Interaction)

ABSTRACT

A numerical model is used to study fault stress and slip near Hollister, California. The geometrically complex system of interacting faults, including the San Andreas, Calaveras, Sargent, and Busch faults, is approximated with a two dimensional distribution of short planar fault segments in an elastic medium. The steady stress and slip rate are simulated by specifying frictional strength and stepping the remote stress ahead in time. The resulting computed fault stress is roughly proportional to the observed spatial concentration of small earthquakes, suggesting that the distinction between segments characterized by earthquakes and those with active creep results, in part, from geometry. A nonsteady simulation is made by introducing, in addition, stress drops for individual moderate earthquakes. A close fit of observed creep with calculated slip on the Calaveras and San Andreas faults suggests that many changes in creep rate (averaged over several months) are caused by local moderate earthquakes. In particular, a three year creep lag preceding the August 6, 1979, Coyote Lake earthquake on the Calaveras fault seems to have been a direct result of the November 28, 1974, Thanksgiving Day earthquake on the Busch fault. Computed lags in slip rate preceding some other moderate earthquakes in the area are also due to earlier earthquakes. Although the response of the upper 1 km of the fault zone may cause individual creep events and introduce delays, the long term rate appears to reflect deep slip.

INTRODUCTION

The relation between observed surface fault slip and earthquakes has been unclear. Coseismic surface faulting is sometimes observed with shallow tectonic earthquakes, for example the 1906 San Francisco earthquake. But often ruptures from moderate earthquakes do not break the surface. Relatively little coseismic surface slip was observed for the 1966 Parkfield, California, earthquake (M =5.6) even though aseismic surface slip was observed both before (Allen and Smith, 1966) and after (Scholz et al., 1969) the earthquake.

In central California surface fault creep seems to be influenced by fault slip immediately below in the depth range of seismicity (4-12km). Creepmeters often record small abrupt movements at the times of or shortly after nearby moderate earthquakes (Tocher, 1960; Bufe and Nason, 1973; Burford et al., 1973). Others show either an increased or decreased creep rate before or after earthquakes (King et al., 1977; Burford et al., 1973; Nason, 1973; Burford, 1976). Some correlations between creep and earthquakes may not be apparent, particularly when the earthquake is on a different fault than the creepmeter. The correlation can be further obscured by delays introduced by the shallow fault zone material.

In this paper I present a theoretical model for fault slip on the San Andreas, Calaveras, Sargent, and Busch faults near Hollister, California. In the first section I describe the model and the numerical method for solving for fault slip. Next, I describe a simulation of steady fault slip and stress accumulation representing an average over 10 years or more. Computed fault

stress is determined, in part, by fault geometry. Furthermore, the computed stress and energy dissipation on the faults appear to be correlated with the observed spatial density of small earthquakes. Finally, episodic slip is superimposed onto the steady model by introducing stress drops for all earthquakes greater than local magnitude 4.0. In spite of its simplicity, the model, which is based on frictional sliding in the brittle seismic depth range, reproduces many of the temporal features of observed surface slip, including changes in creep rate, transient fault locking, and coseismic steps.

THE MODEL

Sections of the San Andreas, Calaveras, and Sargent faults (Brown, 1970) are shown in Figure 1a. The location of the Busch fault was inferred from the main shock focal mechanism and aftershock locations of the November 28, 1974, earthquake (M_L = 5.1) (Savage et al., 1976). An obvious feature of the map is the geometric complexity of the faults over a wide range of length scales. There are four major faults at four quite different orientations; each of these consists of many individual segments with offsets and changes in strike. In modeling the stress and slip on these faults I have assumed that the trace geometry is representative of the fault below the surface, at least down to the lower depth of brittle seismicity (12 km). In support of this Bakun and others (1980), for example, have found good correlation between trace geometry and epicenter locations, directivity, and aftershock clustering.

The faults are modeled as cuts in an otherwise homogeneous linear elastic body of infinite extent. The models are two-dimensional in map view, and the calculations assume plane strain deformation. (Alternatively, the model can be interpreted as plane stress deformation of a thin elastic plate with through-going cuts). Homogeneous stresses are applied at infinity; a stress-slip boundary relation is specified on the faults; and the resulting fault slip is found numerically.

Important limitations of the model are that the crust is not purely elastic nor homogeneous, and faults are not two-dimensional. Inelastic deformation (as evidenced by compression ridges, sag ponds, and permanently deformed rocks) and secondary fracturing relieve stresses, eventually, at discontinuities in the fault (Segall and Pollard, 1980). Although en echelon offsets are sites of inhibited slip, over some sufficiently long time scale the displacement across the fault zone is everywhere essentially uniform. In contrast, fault discontinuities in a two dimensional elastic model form permanent and unrealistic barriers to fault slip. Delaney and Pollard (1980) have found that sets of echelon dike segments sometimes deform as a single long segment due to inelastic deformation at closely spaced segment ends or due to coalescence into one segment just below the surface. Separate fault segments may coalesce below the surface although the depth and geometry are unknown (Segall and Pollard, 1980).

In constructing the two dimensional models I have assumed that the spatial and temporal patterns of crustal deformation and fault interaction, on scales longer than a few kilometers and several months, are governed primarily by

fault slip at the depths of observed seismicity (4-12 km). Aseismic slip above (i.e., surface creep) and below is assumed to follow passively. Furthermore I have assumed that the slip in the seismic depth range is best modeled by joining the separate segments within each of the four major faults to form crooked, though continuous cuts.

The vertical lithostatic pressure gradient and spatial variations of crustal stiffness are ignored for computational economy and also to model only the first order effects that result from fault geometry. Irwin and Barnes (1975) argue that the spatial patterns of fault creep and seismicity in this region are correlated with, if not controlled by, spatial variations of rock type. They suggest that variations of pore pressure and composition in the fault zone might cause variations in fault zone sliding behavior. Such variations could be included in the homogeneous elastic fault model in the form of boundary conditions on the fault surfaces, but have not been included for this paper.

The elastic boundary value problem is solved using the displacement discontinuity method, which is described in detail by Crouch (1976). The method uses Green's functions relating tractions and displacements along the prescribed cuts in the infinite body. The continously varying slip on each fault is approximated (for numerical purposes) by dividing the fault into many short planar segments, each having uniform slip. The various segments can have arbitrary length and orientation, and can be intersecting or not. By choosing the segments to be sufficiently short, geometric complications, such as steps and bends, are approximated to desired accuracy at the expense of

longer computation time. Because each segment has uniform slip, it is identical to a pair of elastic edge dislocations, sharing a common slip (glide) plane and having equal and opposite Burger's vectors.

The advantage of this method is that only the faults have to be discretized. The Green's functions are exact elastic solutions everywhere in the body for a given fault slip. Finite difference and finite element procedures, on the other hand, require that the entire elastic body be discretized, both on and off the fault, with the elastic field equations approximated everywhere by a system of algebraic equations. Furthermore, constructing the solution from the known analytic solutions (Greens functions) saves computation time because the two-dimensional problem is reduced to a one-dimensional one.

The numerical problem is solved as follows. At any point in the body, in particular at the center of the jth segment, the shear stress in the plane of the fault τ_j is the sum of the remotely applied shear stress τ^A_j resolved in the plane of the jth segment plus the stress perturbations resulting from slip u_i on each of the N segments; i.e., the stress due to each pair of dislocations. Because the material is linear elastic the stress due to each segment is simply proportional to the slip on that segment. That is,

$$\tau_j = \tau^A_j + \sum_{i=1}^{N} A^t_{ji}\, u_i \qquad (1)$$

where A^t_{ji} are constant coefficients, that depend on the elastic moduli,

the segment lengths and orientations, and the distance between the ith and jth segments. Similarly, the normal stress on the jth segment σ_j is the sum of the resolved normal component of applied stress σ_j^A plus the perturbations resulting from slip on each segment

$$\sigma_j = \sigma_j^A + \sum_{i=1}^{N} A_{ji}^n u_i \qquad (2)$$

where A_{ji}^n are a second set of coefficients depending on the elastic moduli, the segment lengths and orientations, and the distances between the ith and jth segments. The stress fields associated with elastic dislocations, from which A_{ji}^t and A_{ji}^n can be derived, are well known (Weertman and Weertman, 1964). Crouch (1976) has derived A_{ji}^t and A_{ji}^n for arbitrary segment size and orientation.

We specify the fault strength on each segment as an arbitrary function of slip or normal stress. For example, in this paper the fault strength is chosen to be proportional to normal stress on the fault. That is, for segments that are slipping

$$\begin{aligned} |\tau_j| &= -f_j\sigma_j, \quad \text{if } \sigma_j<0 \\ \tau_j &= 0, \quad \text{if } \sigma_j \geq 0 \end{aligned} \qquad (3)$$

This is mathematically like simple friction (static = dynamic) with a coefficient of friction f_j that may be different on each segment. A more sophisticated model might include a strain hardening and softening fault strength in order to predict instability. This is also where one could include the effects of pore pressure and fault zone composition on the sliding behavior.

For a given set of applied stresses the equations (1), (2), and (3) are solved numerically. A computer program, published by Crouch (1976), computes the influence coefficients A_{ji} and solves the linear equations (1) and (2) numerically. The program has been modified for the present study to include the nonlinearity introduced with the frictional boundary conditions (3).

STEADY SIMULATION

The first model simulation approximates the average distributions of fault slip and stress accumulation in the Hollister area appropriate to the last 10 years or so. The model, shown in Figure 1b, consists of 9 straight cuts chosen to approximate some of the larger changes in fault strike. The model trace is smoother than the mapped geometry in Figure 1a to emphasize the large scale interactions. In the numerical calculations these cuts are further divided into a total of 53 segments (53 pairs of dislocations) of approximately equal length (~2.3 km), each having uniform slip. The portion of the Sargent fault and the northern limit of the San Andreas fault modeled in Figure 1b correspond to faults with significant seismicity in the last 10 years. The locked portion of the San Andreas fault, which slipped in 1906, is left out of the model. (No attempt was made to determine whether or not the locking is a geometric effect.) The northern end of the Calaveras fault and the southern end of the San Andreas fault were terminated arbitrarily to save computation time, though both faults are active beyond the limits chosen for the model. Uniform confining pressure and shear stress are applied remotely

with the direction of maximum shear stress far from the faults oriented parallel to the local strike of the plate boundary (325°) given by Minster and Jordan (1978). The remote shear stress is stepped ahead uniformly in time resulting in steady rates of slip and of stress accumulation. Simple friction (static = dynamic) is assumed on the faults, so that no episodic behavior (viz., individual earthquakes) is modeled.

The results are shown in Figure 2. In the center of the figure is a seismicity map for the 10 years 1970-1979 showing earthquakes with magnitude greater than 2. At the top of the figure computed slip rate and shear stress along the Calaveras fault are plotted at the same scale as the map directly below. At the bottom of the figure, stress and slip rate along the San Andreas and Sargent faults are shown.

Slip rate is computed by successively increasing the remote shear stress and finding the difference in the static fault displacement between any two successive time steps. At very low shear stress some of the segments slip, and some remain frictionally locked, depending on the segment orientation. As the shear stress is increased, more of the segments slip causing non-steady, generally increasing, slip rates. Finally, when all segments are slipping, further steady increases in stress give the steady slip rates plotted in Figure 2.

The computed slip rate is proportional to the applied stress loading rate. The proportionality, however, is model dependent. For faults of finite extent in an infinite body, as modeled here, the slip rate is also roughly proportional to the fault length. Including more of the active portions of

the San Andreas and Calaveras faults increases the computed slip rate. For the model in Figure 1b, an applied shear stress loading rate of 0.3 bar/year scales to a computed maximum slip rate of 20 mm/year on the Calaveras fault (for shear modulus $\mu = 6 \times 10^5$ bar). An additional caution is that terminating the northern extent of the Calaveras fault and the southern extent of the San Andreas fault causes the modeled slip rate to be artificially low near those ends.

The slip rates in Figure 2 were computed for the two friction coefficients, f=0 (no friction) and f=0.6. The slip rate is similar in the two cases except that increased friction decreases slip on the San Andreas fault and increases it on the Calaveras fault. This results from the orientations and the assumed dependence of fault strength on compressive stress. The normal to the San Andreas fault is oriented more toward the greatest compressive principal stress; the Calaveras, toward the least compressive. The slip rate is also influenced by fault interaction. The computed slip rate distribution from north to south along the San Andreas shows a pronounced dip just north of the junction with the Calaveras fault and a large increase to the south. A simple-minded explanation is that to the north the right lateral slip needed to accommodate the relative plate motion is distributed across both faults, while to the south only the San Andreas slips.

The computed shear stress on each fault segment is a function of the remotely applied normal and shear stresses, the fault strike, and the fault slip distribution everywhere in the system. Although the slip rate is steady

everywhere, the stress is not. The shear stresses shown in Figure 2 are for two successive time steps, two years apart, for the case f=0.6. The difference between the two is the shear stress accumulation rate, which is proportional to the remote stress loading rate. The trend with time is to increase the stress maxima and to decrease stress minima. Consequently, the various plotted features become exaggerated with time. For example, the peak-to-peak difference in computed shear stress between points A and B grows by ~0.4 bar/year (40 bars in 100 years).

The zero shear stress level in Figure 2 is ambiguous and depends on the assumed value of confining pressure (applied normal stress) and the absolute level of remotely applied shear stress. In general the stress on the San Andreas fault is computed to be larger than on the Calaveras. This is again due to the orientation. The shear stress is proportional to the compressive stress, and the average normal compressive stress is larger on the San Andreas. Note the relatively low stress on the San Andreas just north of the junction with the Calaveras and the high stress just to the south. This large scale variation results from right lateral slip on the Calaveras which tends to compress and lock the San Andreas fault south of the junction and to unlock it to the north.

On the Calaveras fault note the large fluctuations in stress due to the large bend, plus the locking and unlocking influence of left lateral slip on the Busch fault. Smaller scale variations in computed stress occur every time a step or bend is modeled. In fact, a limitation of the model is that uncertainties in fault geometry have a large effect on the estimated stress.

Finally, note the apparent correlation between the spatial density of small earthquakes and computed stress. On the San Andreas fault the seismicity is high south of the junction with the Calaveras where the computed stress is high. This is the region of the 1972 Bear Valley and Stone Canyon earthquakes. North of the junction, where the computed stress is low, the seismicity is low. The model suggests that this is a relatively unlocked region that accumulates stress slowly. Farther north where the computed stress increases, so does the seismicity. One might expect that the seismicity should instead be correlated with the frictional energy dissipation rate, which is the product of the fault shear stress times the slip rate. This appears to be at least qualitatively true in Figure 2. Alternatively, if no assumptions are made about the fault constitutive law it still appears that seismicity is correlated with the modeled normal stress on the fault.

NONSTEADY SIMULATION: 1969-1979

A nonsteady simulation of fault slip during the years 1969-1979 is made by superimposing moderate earthquake stress drops onto a steady simulation. The model, shown in Figure 1c, was constructed by drawing a continuous trace through each of the faults in Figure 1a and dividing these into 55 straight segments. The model is similar to that used for the steady simulation (Figure 1b) but more closely approximates the actual trace geometry.

The calculation is similar to the steady simulation. The 11-year period (1969-1979) is divided into 30 unequal time steps. Simple friction is assumed on the faults; the boundary shear stress is stepped uniformly in time; and the static fault slip and stress are computed at each time step.

The only nonsteady input to the model is the abrupt stress drop, actually a drop in coefficient of friction, specified for each moderate earthquake (local magnitude $\geq$ 4.0) shown in Figure 1c. Each stress drop is imposed on the single model segment closest to the earthquake epicenter and at the time step closest to the actual time of the earthquake. To save computation time events occuring within several months of each other are clustered into a single time step. Events used in the simulation are listed in Table 1. In detail, each earthquake is modeled in two steps. First, the remote boundary stress is advanced through time, and the static fault slip is found everywhere until just before the prescribed stress drop. Then keeping the remote stress fixed, the friction is decreased on the one model segment closest to the epicenter, and the static slip is recomputed everywhere in the system. The change in frictional strength on just one of the 55 segments, with no change in the remote stress, leads to a readjustment of slip throughout most of the fault system. This readjustment, the difference between the static solutions before and after the stress drop, is interpreted as the sum of the coseismic slip plus the aftershocks, creep, and all preseismic and postseismic adjustments. There is no viscous or time dependent element in the model to spread these effects out in time. Consequently, the mainshock seismic moment is only a fraction of the total computed readjustment of the fault system.

Creep Solution

A model solution was developed by adjusting (by trial and error) the remote shear stress loading rate, the starting coefficient of friction, and the

earthquake stress drops until a single simulation gave reasonable agreement to creep records at the five sites shown in Figure 1c and listed in Table 2. The model stress drops were adjusted arbitrarily to improve the fit, regardless of published earthquake moment. A comparison of observed and calculated slip is shown in Figure 3. Time in years is shown on the horizontal axis. The location in time and the magnitude of the modeled earthquakes are shown by the vertical lines along the time axis.

A friction coefficient f = 0.40 was used for the model solution in Figure 3. (In principle, 55 different coefficients on the 55 segments can be adjusted separately, but for simplicity they were kept uniform throughout the model.) Smaller coefficients give too large a slip rate on the San Andreas fault relative to the Calaveras, and vice versa for larger coefficients. A different coefficient, however, might be more appropriate for a different fault geometry or different orientation of the remote principal stresses.

The calculated slip and the creep data to which the model was fit are now discussed at each creepmeter. Many of the steps and long term changes in creep rate are reproduced by the model. Most individual creep events are not.

SHR1 The computed slip history at the site of creepmeter SHR1 resembles the observed creep record, but the comparison is more obvious if the computed slip is shifted (delayed) by 9 months (Figure 3a). Such a delay might be expected if the surface slip lags behind the slip at seismic depths because of near surface fault gouge or soil conditions. The record begins in 1971. On a gross scale both the observed (dots) and computed (solid) curves are concave upward until mid-1972, followed by a concave downward until mid-1974, a

moderate slope during most of 1975, and a flat record after 1975. Looking closer, a few shorter term features seem to match. A slight increase in rate in early 1972 (point A') is correlated with an increase in computed rate beginning at point A. No event is modeled at A; instead, the change is a transient from earthquakes 1, 2, and 3 (Table 1) at Hollister in late 1969 and early 1970. A lower observed rate between B' and D' is correlated with a slight computed decrease starting at B resulting from the Bear Valley earthquake (event 4) and another computed decrease at C from earthquakes 5-8 at San Juan Bautista, Cienega Road, and Stone Canyon. An observed step at D' correlates with a computed step at D from event 11 on the northern Calaveras. A moderate rate starting at E' matches that between E and F. The creep is stopped at F by the sequence of events 13-15 on the Busch fault beginning in November,1974. The observed and computed records are essentially flat for more than 3 years between F'-H' and F-H with a recovery in creep at H and H' in 1978. The flat or locked record appears to be initiated by the November, 1974, earthquake. A distant event is modeled G, with an incrase in stress but no increase in creep rate. The resumption of creep at H marks the point at which the boundary stress has increased to recover from the disturbance created by the November, 1974, earthquake. The lag in creep is discussed more in a later section.

WRT1 The point by point correlation between observed and computed records at WRT1 is not as striking as at SHR1, but a comparison can be made with the computed record, again delayed by 9 months (Figure 3a). Overall, the average creep rate is higher before 1975 (point F') than after 1975 on both the

observed and computed records. The change is roughly correlated with the earthquake sequence on the Busch fault beginning in November, 1974, the same sequence that locked the fault at SHR1. In detail, an increase in rate at A' compares with one at A. A step at B' correlates with one at B. A step and decrease in rate at C' match one at C. Finally a step at D' correlates with a computed step followed by a rapid increase at D. The earthquakes associated with the steps and rate changes at A-F are the same as already discussed for SHR1.

XSJ2 The most striking features of creep at XSJ2 (Figure 3b) are the change from a moderate rate before mid-1972 (point C') to a rapid rate lasting until 1975 and then a return to a moderate rate. The very rapid increase beginning in 1972 correlates with computed steps at B, C, D and E which are directly attributable to events 4-10 (Table 1) along much of the San Andreas fault. Smaller computed steps near F are caused by the Busch fault sequence.

HRS3, CWC3 The two creep meters HRS3 and CWC3, only 3 km apart, are modeled by the same model segment. Again, the most striking feature of the observed and computed records (Figure 3b) is the change from a relatively low rate before 1972 to a fast rate lasting to 1975, then a return to a low rate. A very slight decrease at A' is caused by earthquakes 1 and 2 at Hollister. The rapid creep between B' and E' is correlated with the computed steps at B, C, D and E which are directly attributable to events 4-10 all along the San Andreas fault.

FAULT SLIP BEFORE THE COYOTE LAKE EARTHQUAKE

Burford (1976) has pointed out that many moderate earthquakes on the active portion of the San Andreas fault are preceded by precursory periods of anomalously low creep rates. There is some evidence that the rate recovers again shortly before some earthquakes. Similarly, Raleigh et al. (1979) have noted that the three year lag in creep at SHR1 on the Calaveras fault might be a precursor to the August 6, 1979, Coyote Lake earthquake. Because the model simulation discussed earlier reproduces the SHR1 creep lag quite well, we can use the model to study the locking process.

The computed stress at SHR1 is plotted with the creep records in Figure 3a. Before the November, 1974, earthquake the computed shear stress equals the frictional stress at SHR1. This is just the boundary condition, equation (3), for any segment that is slipping. At the time of the earthquake the left lateral slip on the Busch fault increases both the normal stress (i.e., the friction) and the applied shear stress. The increase in friction is greater, so the patch becomes locked. The model predicts that slip resumes again in 1978 (point H) when the shear stress has increased enough to meet the friction. The length of the locked period depends on the slip of the Busch fault earthquakes. Larger slip causes a greater increase in friction at SHR1, which takes longer to recover.

The computed slip, averaged over 30 km of the Calaveras fault (8 model segments between points A-A' in Figure 1c), is compared with the geodetically

determined average slip (N. King et al., 1980) for the same region in Figure 4. The observed geodetic slip follows a nearly linear trend (slightly concave upward) beginning in mid-1971 until late 1974. A decrease in rate occurs in early 1975, followed by a gradual increase in slip rate for about 4 1/2 years. The apparent large change in geodetic slip rate in 1978, one year before the earthquake, may not be real (W. Prescott, pers. com.) because it is defined by only the single 1978 value. The computed record shows some of the same features. (Note, however, that the computed rate, which was matched to creep, is generally 50-60% of the geodetic rate, suggesting that creepmeters capture only that fraction of the total block offset across the Calaveras fault.) The Busch fault earthquakes lock or decrease the slip rate on much of the Calaveras beginning in November, 1974. The locking gradually recovers on more and more segments, causing the average slip to be concave upward.

In summary, a period of decreased fault slip rate beginning in 1975 at creepmeter SHR1 and a questionable one in 1978 detected by geodolite measurements, preceded the 1979 Coyote Lake earthquake. There is no proof that these are precursors to the earthquake, but they do fit the pattern of precursory creep lags suggested by Burford (1976) for earthquakes on the San Andreas fault. The model results suggest that the creep lag beginning in 1975 was directly caused by the 1974-1975 earthquakes on the Busch fault. While only simple friction is included in the model, it appears that a rate-dependent (or aging) fault law, which causes strength to increase with decreased slip rate (Dieterich, 1979) would enhance the locking and possibly lead to instability. Even without such a law, it seems likely that the Coyote Lake earthquake was not an entirely random or spontaneous event, but rather a direct result of conditions set up by the November 1974 earthquake.

COMPUTED SLIP BEFORE OTHER EARTHQUAKES

The pattern of creep lags in an epicentral region caused by prior earthquakes is evident for several other events in the simulation. Computed slip histories at the epicenters of modeled events 5-9, 12-15, 17, and 18 are plotted in Figure 5. Creepmeters are not available at many of these sites, so it is important to remember that these are only model results. The slip at events 1-3 is not plotted because the events occur too early in the simulation for their preseismic slip to be examined. Events 4, 10, 11, and 16 are not plotted because they lie close to the model edges and may be influenced by events just outside the model that are not included. The star on each computed curve marks the time of the earthquake occuring at that model segment.

The fault at the site of the January, 1974, earthquake on the Sargent fault (event 12) is locked beginning in late 1969 (point A), by the 1969-1970 events at Hollister. In this case locking occurs because the frictional stress is increased by the events, while the shear stress is relaxed. The creep rate begins to recover in late 1970 (point B), but decreases again in late 1973 (point C), apparently due to earthquake 11 in 1973 on the Calaveras fault.

The computed slip before events 6-8, near San Juan Bautista (plotted for two adjacent model segments), becomes locked beginning in late 1969-early 1970 (point D) due to events 1-3 near Hollister. The locking occurs because the shear stress is slightly relaxed by the earthquakes, while the friction stays

essentially the same. The computed creep rate begins to increase in late 1970 and is nearly up to the 1969 rate when the earthquakes 6-8 occur in late 1972. Events 5 and 9 farther south on the San Andreas are preceded by very slight (perhaps insignificant) decreases in computed creep rate (points E and F). Again the creep rate is recovered up to the 1969 rate during the year before the earthquakes.

The computed slip at the epicenter of the August 6, 1979, earthquake on the Calaveras fault (event 18) shows a slight decrease in slip rate at points G and H. Event 11 occurred ~11 km to the northwest at point J. A very slight decrease in slip rate occurs at point K resulting from the Busch fault earthquakes, but the locking is not nearly as prounounced as that measured at the SHR1 creepmeter 20 km to the southeast.

The computed creep on the Busch fault (events 13-15) is stopped in late 1969-early 1970 (point L) by the Hollister earthquakes. In this case readjustments following the Hollister events decrease both the frictional stress and shear stress on the Busch fault, but the shear stress decreases faster, causing the locking. Creep on the Busch fault begins again in late 1970 but stops again in early 1974 (point M) following the January, 1974, earthquake on the Sargent fault.

To summarize, the model predicts periods of lower than average slip rate preceding some of the moderate earthquakes in the simulation. The computed low slip rates are caused by earthquakes elsewhere in the simulation. Whether or not these low rates are premonitory or part of the failure process cannot be determined, however, since the model cannot predict instability.

DISCUSSION AND CONCLUSIONS

A theoretical model has been presented for fault slip and stress on interacting faults near Hollister, California. The results of a steady simulation suggest that the observed density of earthquakes is correlated with the long term calculated normal stress on the fault, or if simple friction is assumed, with shear stress. Alternatively, the seismicity may be correlated with the computed energy dissipation rate on the fault: actively creeping sections with low levels of seismicity might be those with low computed energy dissipation; sections with higher seismicity, including frequent moderate earthquakes, might be those with higher computed energy dissipation. Thus, the distinction between actively creeping faults with minor seismicity and faults with larger earthquakes might be due to geometry.

A nonsteady simulation of slip during 1969-1979 is made by superimposing stress drops from moderate earthquakes onto an otherwise steady model. The simulation is matched to creep data by adjusting the remote stress loading rate, coefficient of friction, and the earthquake stress drops. The simulation reproduces many long term features of observed slip including coseismic steps, changes in creep rate, and transient fault locking; individual creep events are not predicted. The close agreement leads to several conclusions:

(1) Trends in surface creep seem to mimic the slip expected in the depth range of brittle seismicity, although the response of the shallow fault zone material may introduce a delay.

(2) The slip model adjusted to match fault creep at 5 sites resembles changes in long term geodetic slip rate averaged over 30 km of the Calaveras fault. The geodetic slip is nearly a factor of 2 larger, however, suggesting that only a fraction of the fault zone is sampled by creepmeters on the Calaveras fault.

(3) The modeled slip rate at most points is influenced by most of the larger earthquakes lying within several 10's of kilometers, even when those earthquakes are on other faults. That is, the various faults seem to interact.

(4) It has been suggested (Burford, 1976) that many moderate earthquakes along the San Andreas fault in central California are preceded by periods of anomalously low creep rate. The model results predict a decrease in slip rate before some earthquakes, and in each case, these are the direct result of an earthquake somewhere else in the fault system. In particular the model reproduces quite well the decrease in slip rate before the 1979 Coyote Lake earthquake and indicates that the decrease was a direct result of the 1974 sequence of earthquakes on the Busch fault.

Acknowledgements: Frequent discussions with Bill Stuart were helpful.

REFERENCES

Allen, C. R. and S. W. Smith, Parkfield earthquakes of June 27-29, Monterey and San Luis Obisbo Counties, California. Pre-earthquake and post-earthquake surficial displacements, Bull. Seismol. Soc. Am., 56, 966-967, 1966.

Bakun, W. H., R. M. Stewart, C. G. Bufe, and S. M. Marks, Implication of seismicity for failure of a section of the San Andreas fault, Bull. Seismol. Soc. Amer., 70, 185-202, 1980.

Brown, R. D., Faults that are historically active or that show evidence of geologically young surface displacement, San Francisco Bay Region. A progress report: Oct. 1970, U.S. Geol. Surv. Misc. Field Studies Map MF-331, 1970.

Bufe, C. G. and R. D. Nason, Creep, strain, and seismicity in the vicinity of Stone Canyon Observatory, Earthquake Research in NOAA, 1971-1972, Tech. Rep. ERL256-ESL28, NOAA, Boulder, Co. 1973.

Burford, R. O., S. S. Allen, R. J. Lamson, and D. D. Goodreau, Accelerated fault creep along the central San Andreas fault after moderate earthquakes during 1971-1973, Proceedings of the Conference on Tectonic Problems of the San Andreas Fault System, Stanford Univ. Publ. Geol. Sci., 13, 268-2744, 1973.

Burford, R. O., Fluctuations in rates of fault creep associated with moderate earthquakes along the central San Andreas fault, EOS Trans., Am. Geophys. Un., 57, 1012, 1976.

Crouch, S. L., Solution of plane elasticity problems by the displacement discontinuity method, Internat. Jour. for Numerical Methods in Engineering, 10, 301-343, 1976.

Delaney, P. T. and D. D. Pollard, Deformation of host rocks and flow of magma during growth of minette dikes and breccia-bearing intrusions near Ship Rock, New Mexico, U.S. Geological Survey Professional Paper, in press, 1980.

Dieterich, J. H., Modeling of rock friction. 1. Experimental results and constitutive equations, J. Geophys. Res., 84, 2116-2168, 1979.

Irwin, W.P. and I. Barnes, Effect of geologic structure and metamorphic fluids on behavior of the San Andreas fault system in central and northern California, Geology, 713-716, 1975.

King, C.-Y., R. D. Nason, and R. O. Burford, Coseismic steps recorded on creep meters along the San Andreas fault, J. Geophys. Res., 82, 1655-1661, 1977.

King, N. E., J. C. Savage, M. Lisowski, and W. H. Prescott, Preseismic and coseismic deformation associated with the Coyote Lake, California, earthquake, J. Geophys. Res., 86, B2, 892-898.

Minster, J. B. and T. H. Jordan, Present day plate motions, J. Geophys. Res., 83, B11, 5331-5354, 1978.

Nason, R. D., Fault creep and earthquakes on the San Andreas fault, Proceedings of the Conference on Tectonic Problems of the San Andreas Fault System, Stanford Univ. Publ. Geol. Sci., 13, 275-285, 1973.

Raleigh, B., W. Stuart, and P. Harsh, Creep on the Calaveras Fault near Coyote Lake, EOS Transactions, American Geophysical Union, 60, 46, 890, 1979.

Savage, J. C., M. A. Speith, and W. H. Prescott, Preseismic and coseismic deformation associated with the Hollister, California, earthquake of November 28, 1974, J. Geophys. Res., 81, 3567-3574, 1976.

Scholz, C. H., M. Wyss, and S. W. Smith, Seismic and aseismic slip on the San Andreas fault, J. Geophys. Res., 74, 2049-2069, 1969.

Segall, P. and D. D. Pollard, Mechanics of discontinuous faults, J. Geophys. Res. (in press), 1980.

Tocher, D., Creep rate and related measurement at Vineyard, California, Bull. Seismol. Soc. Amer., 50, 396-404, 1960.

Weertman, J. and J. Weertman, Elementary Dislocation Theory, 213 pp., MacMillan Co., New York, 1964.

Figure Captions

Figure 1: (a) Portions of the San Andreas, Calaveras, Sargent, and Busch faults near Hollister, California (from a map by Brown (1970)). (b) Model of the faults in (a) for the steady simulation. Tic marks show the 53 individual segments. Dashed arrows show the orientation of the maximum remote shear stress. (c) Model of the faults in (a) for the nonsteady simulation. Triangles with dates show epicenters for earthquakes with magnitude greater than 4. Open circles are creepmeters. Letters A-A' mark the section of the Calaveras fault described in Figure 4.

Figure 2: Results of the steady simulation. Map in the center shows epicenters for earthquakes larger than magnitude 2 during 1970-1979. At the top, computed fault shear stress and slip rate are plotted as a function of position along the Calaveras fault. Plots and map have the same distance scale. At the bottom, shear stress and slip rate are plotted for the Sargent and San Andreas faults. Stress plots compare two time steps in a simulation with coefficient of friction f = 0.6: closed circles first, compared sith open circles two years later. Slip rates are shown for two different simulations with coefficients of friction f = 0 and f = 0.6.

Figure 3: Comparison of observed fault creep with fault slip computed from the nonsteady simulation. The horizontal axis is time in years. Vertical

lines along the time axis show the time and magnitude of earthquakes used in the simulation. Large open and closed circles on the time axis show times of computational time steps; the closed circles represent time steps with specified stress drops (a) Observed and computed fault creep at creepmeters SHR1 and WRT1 on the Calaveras fault. Dotted curve is observed creep. Dashed curve is computed slip. Solid curve shows the computed slip delayed 9 months. In addition, computed fault shear stress (solid curve) and frictional stress (dashed curve) at SHR1 are shown at the top. (b) Observed (small dots) and computed (dashed curves) slip at creepmeters XSJ2, HRS3, and CWC3 on the San Andreas fault.

Figure 4: Comparison of geodetically determined slip (N. King et al., 1980) and computed slip on Calaveras fault. Large dots show the times of geodetic surveys.

Figure 5: Modeled fault slip prior to several moderate earthquakes computed at the epicenters of those earthquakes. The top curve shows the computed slip near the epicenter of event 12 (Table 1) on the Sargent fault. The second and third curves show the slip on two adjacent model segments near the epicenters of events 6-8 near San Juan Bautista. The fourth curve shows slip near the epicenter of event 9, and so on. The star on each curve shows the time of the earthquake occuring at that site. Letters A-M mark features refered to in the text.

Table 1. Earthquakes included in the nonsteady simulation.

	Date (yr.mo.day)	Time (GMT)	Lat.	Long	Depth (km)	Mag.*
1	691027	1059	36 47.48	121 22.65	10.9	4.5
2	691115	2058	36 46.24	121 21.78	11.3	4.1
3	700331	0702	36 52.06	121 24.47	11.3	4.5
4	720224	1556	36 34.69	121 12.54	7.5	5.0
5	720904	1804	36 37.48	121 16.46	5.7	4.6
6	720923	1507	36 47.58	121 31.57	6.8	4.1
7	721003	0630	36 48.15	121 31.73	5.0	4.8
8	721003	1110	36 48.82	121 32.71	5.1	4.0
9	730115	0943	36 40.32	121 20.02	6.3	4.1
10	730622	0129	36 33.79	121 12.29	9.6	4.2
11	731003	1007	37 12.26	121 35.12	4.7	4.6
12	740110	1122	36 57.08	121 35.71	7.7	4.3
13	741128	2301	36 54.96	121 28.68	5.8	5.1
14	741231	2022	36 55.96	121 28.01	8.7	4.3
15	750303	1134	36 56.03	121 28.25	7.8	4.2
16	771215	1115	36 35.00	121 13.50	10.0	4.2
17	790802	2143	36 48.34	121 32.64	5.0	4.0
18	790806	1705	37 6.59	121 30.68	6.8	5.9

events 1-16 have local magnitudes; evnets 17 and 18 have coda magnitudes.

Table 2. Creepmeters compared with the nonsteady results.

	Latitude	Longitude
CWC	36°45.0'	121°23.1'
HRS	36°46.3'	121°25.3'
SHR	36°56.6'	121°26.7'
WRT	36°52.2'	121°24.8'
XSJ	36°50.2'	121°31.2'

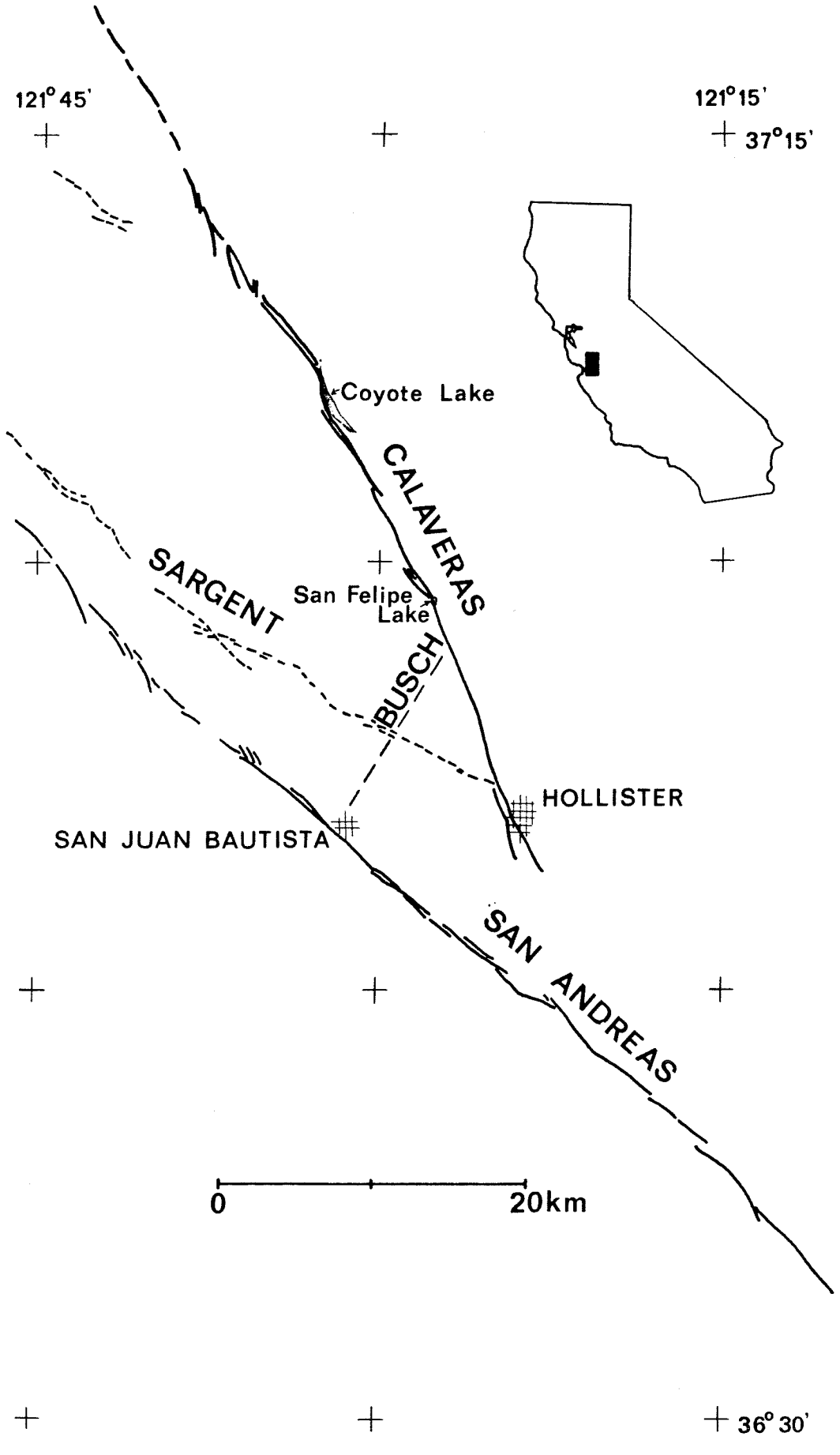
121°45'
121°15'
37°15'
Coyote Lake
CALAVERAS
SARGENT
San Felipe Lake
BUSCH
HOLLISTER
SAN JUAN BAUTISTA
SAN ANDREAS
0
20km
36°30'

a

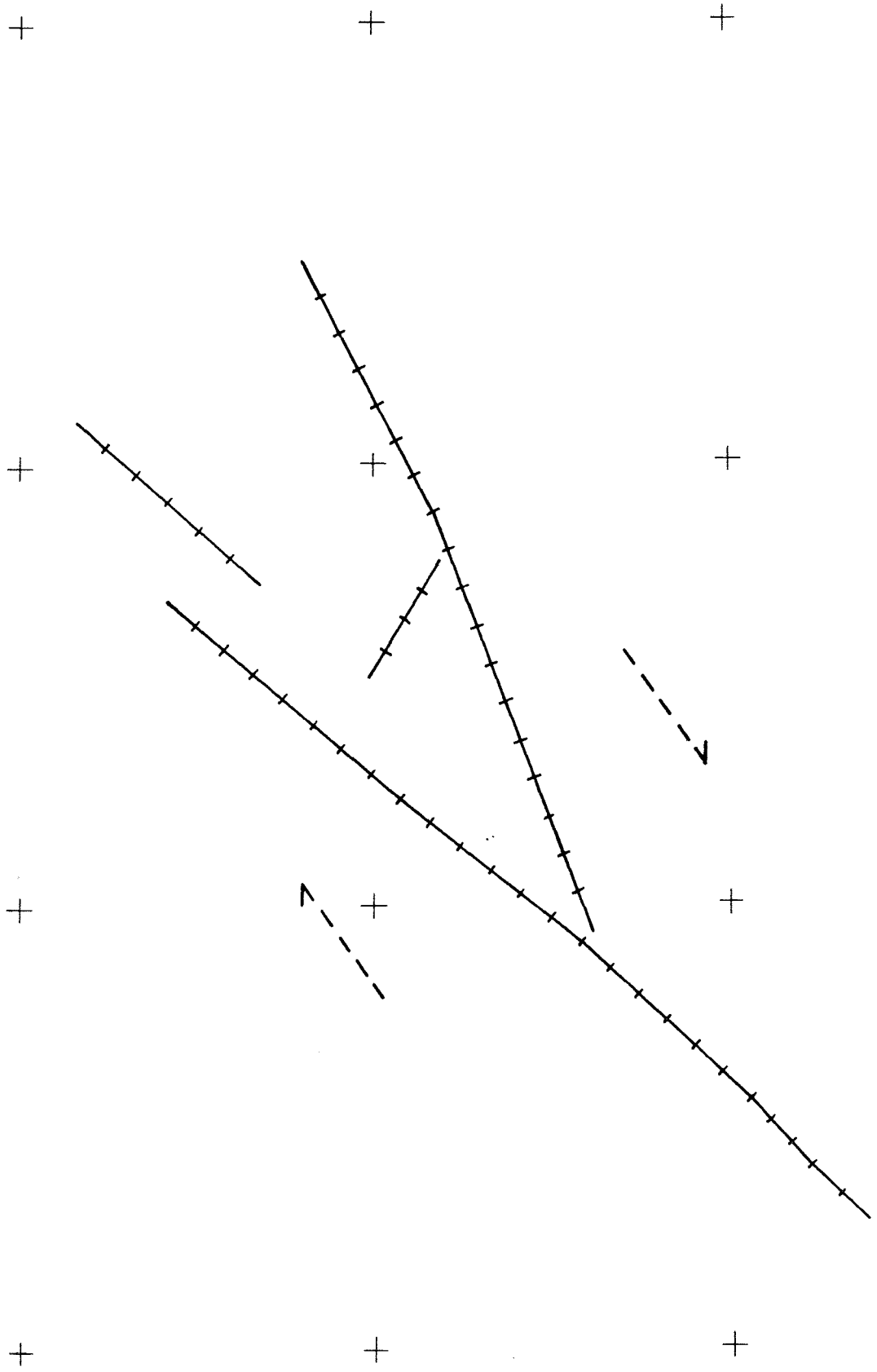

b

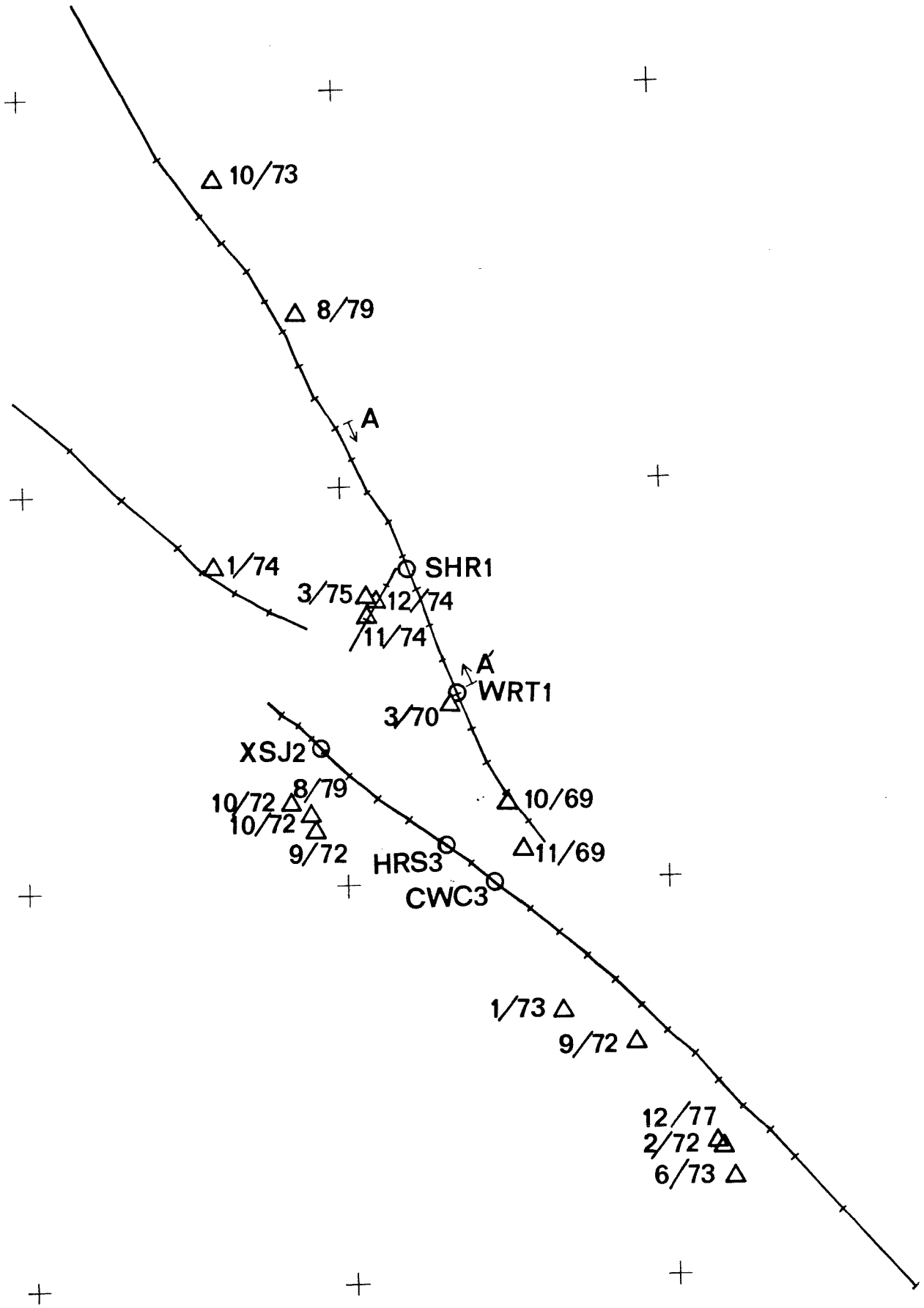
10/73
8/79
A
1/74
SHR1
3/75
12/74
11/74
A'
WRT1
3/70
XSJ2
8/79
10/72
10/72
9/72
10/69
11/69
HRS3
CWC3
1/73
9/72
12/77
2/72
6/73

c

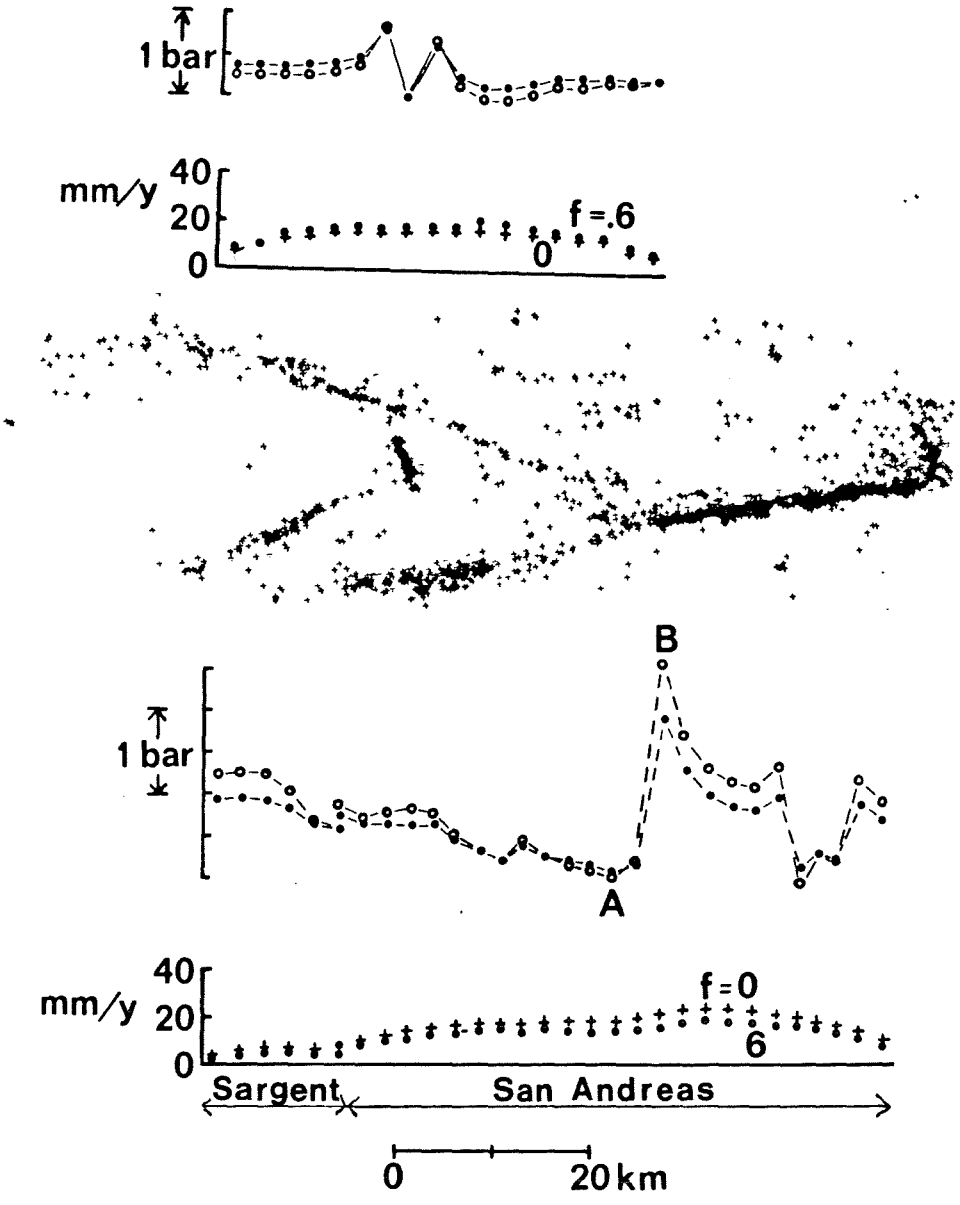
1 bar
mm/y
40
20
0
f=.6
0
B
1 bar
A
mm/y
40
20
0
f=0
6
Sargent
San Andreas
0
20 km

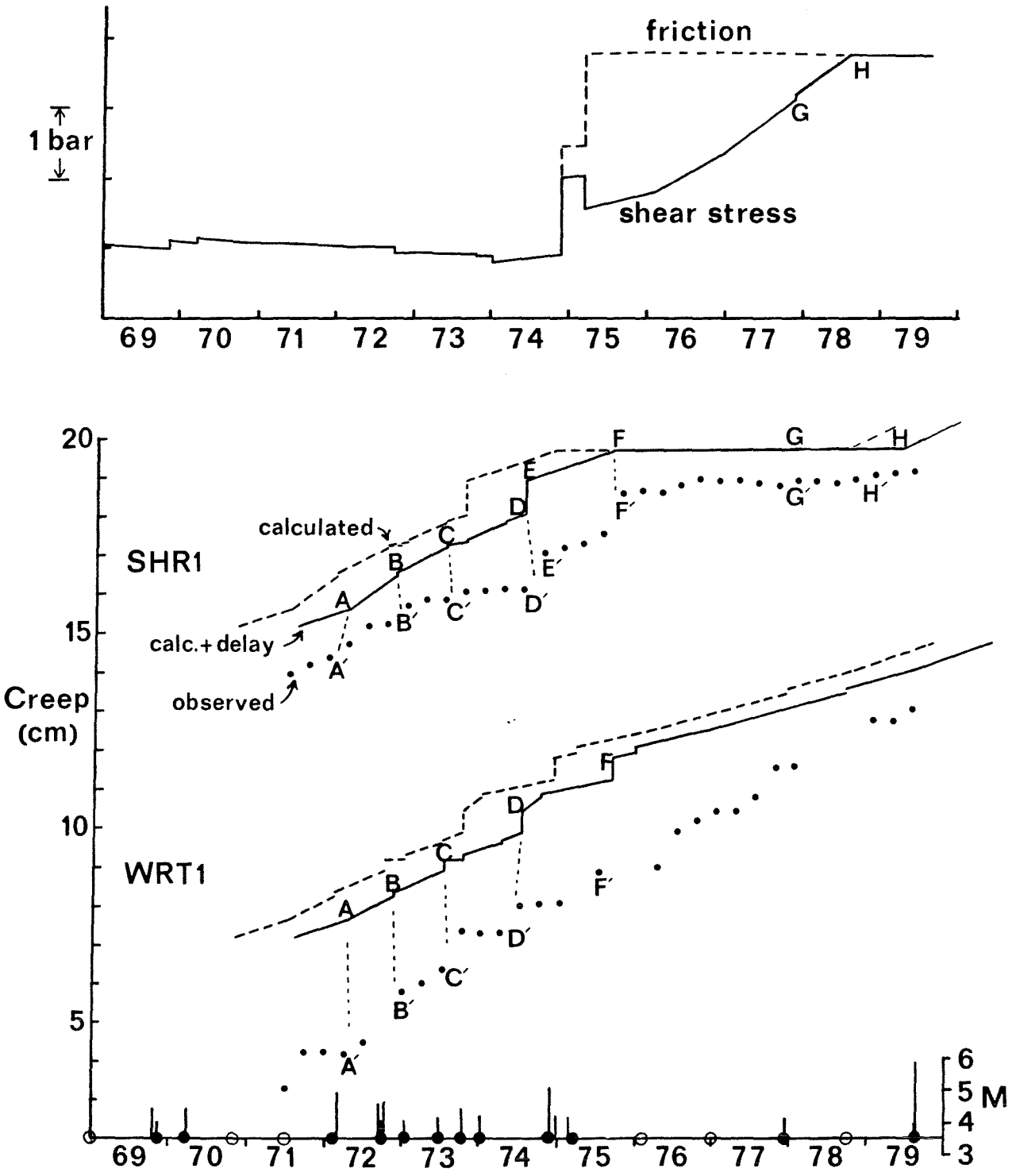
friction
shear stress
1 bar
H
G
69 70 71 72 73 74 75 76 77 78 79
20
15
10
5
Creep (cm)
SHR1
WRT1
calculated
calc.+delay
observed
A
B
C
D
E
F
G
H
6
5
4
3
M

a

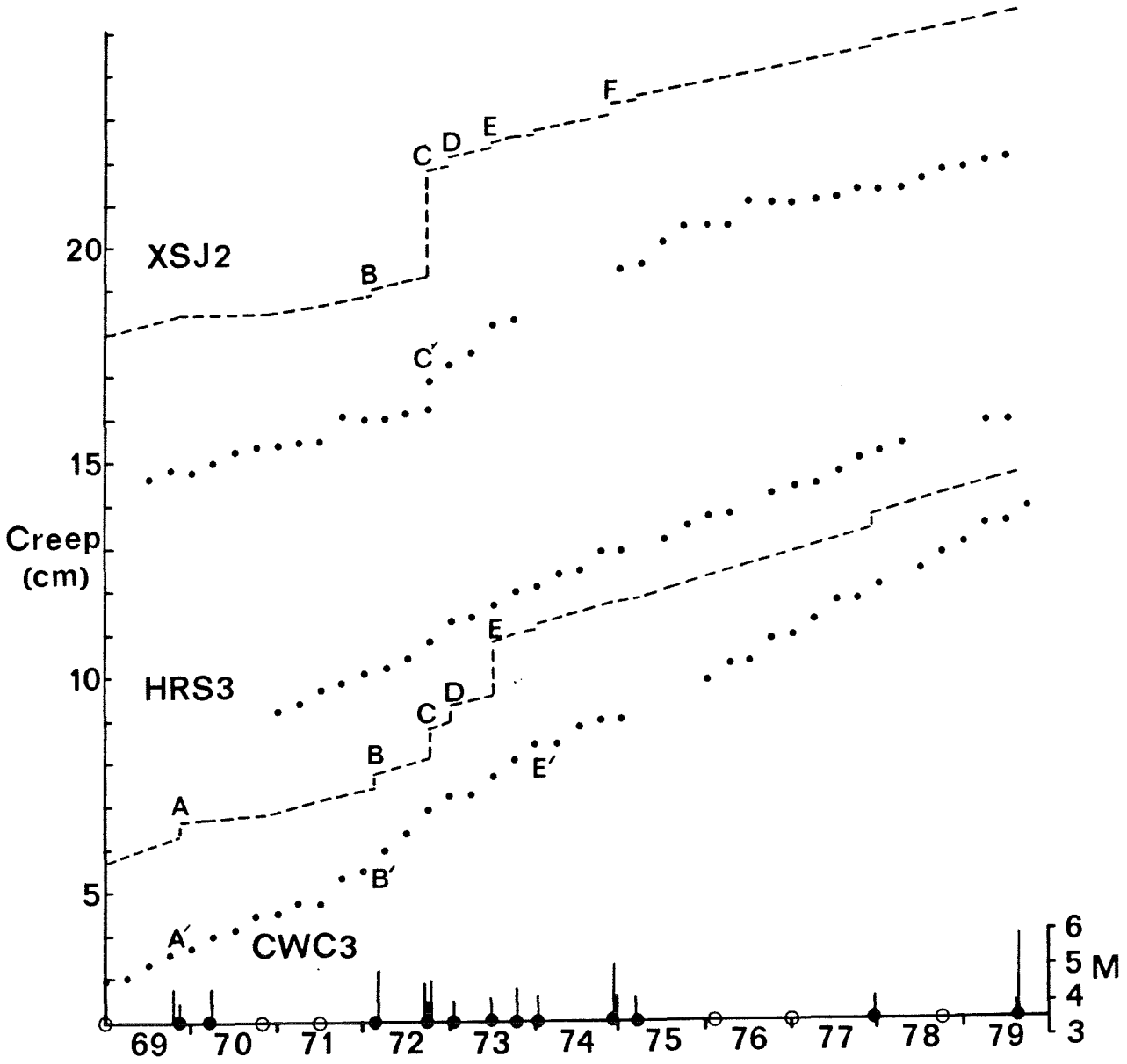
XSJ2
HRS3
CWC3
Creep
(cm)
20
15
10
5
A
B
C
D
E
F
A′
B′
C′
E′
69
70
71
72
73
74
75
76
77
78
79
6
5
4
3
M

b

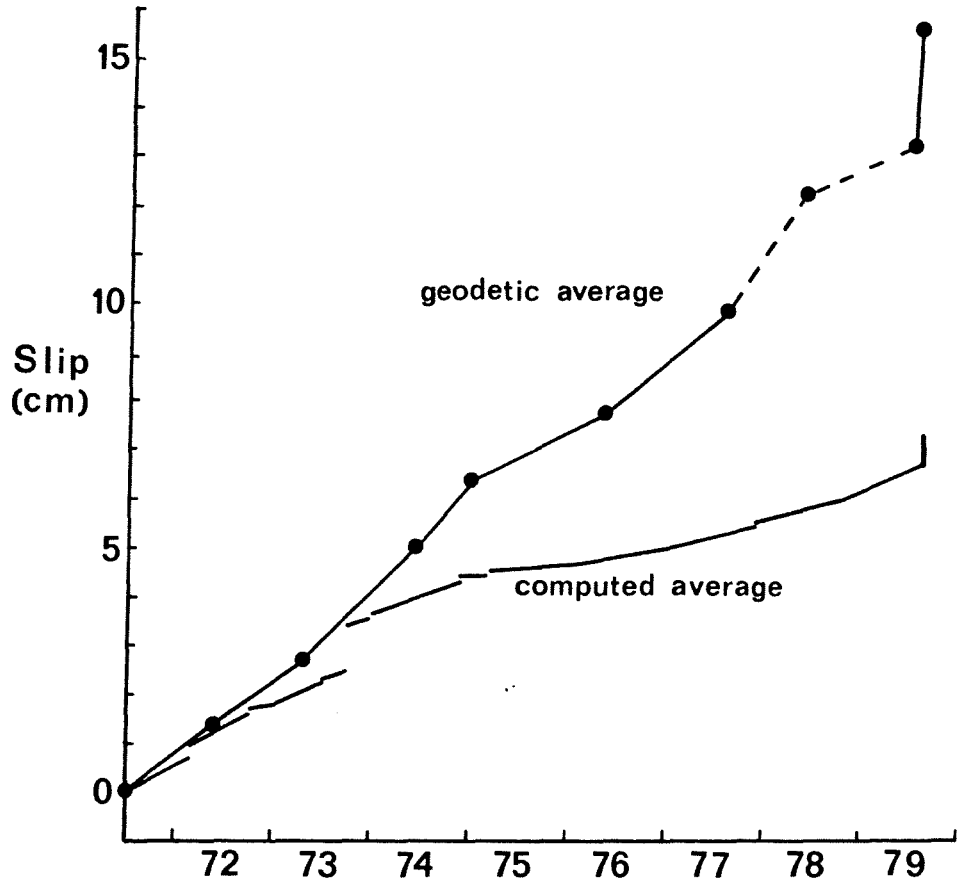
15
10
5
0
Slip
(cm)
geodetic average
computed average
72
73
74
75
76
77
78
79

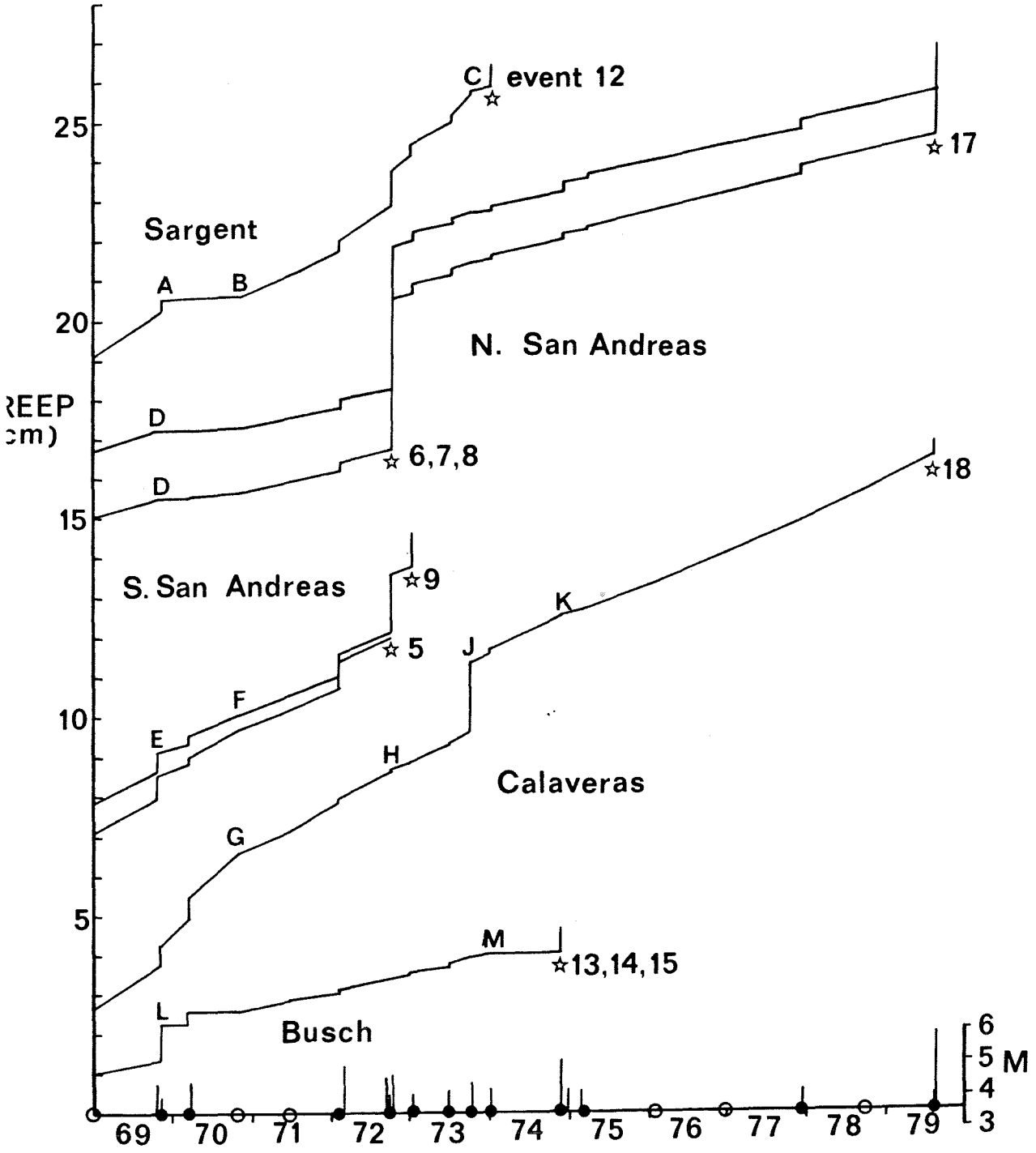
25
20
15
10
5
REEP
cm)
C
event 12
17
Sargent
A
B
N. San Andreas
D
D
6,7,8
18
S. San Andreas
9
5
K
J
F
E
H
Calaveras
G
M
13,14,15
L
Busch
6
5
M
4
3
69
70
71
72
73
74
75
76
77
78
79